

KHL 92051  
Copy 2 R61 RR  
Accn: 2160069

RAL-92-051

Science and Engineering Research Council

# Rutherford Appleton Laboratory

Chilton DIDCOT Oxon OX11 0QX

RAL-92-051

\*\*\*\*\*  
RAL LIBRARY R01  
ACC\_No: 216069  
Shelf: RAL 92051  
R61

## Simulations and Qualitative Analysis of the AMPTE Experiments

F Kazeminezhad R Bingham and J M Dawson

August 1992

LIBRARY, R61  
29 SEP 1992  
RUTHERFORD APPLETON  
LABORATORY

**Science and Engineering Research Council**

**"The Science and Engineering Research Council does not accept any responsibility for loss or damage arising from the use of information contained in any of its reports or in any communication about its tests or investigations"**

# Simulations and Qualitative Analysis of the AMPTE Experiments

F. Kazeminezhad<sup>a</sup>    R. Bingham<sup>b</sup>    J.M. Dawson<sup>a</sup>

May 29, 1992

## ACRONYMS

AMPTE: Active Magnetospheric Particle Tracer Explorers

IRM: Ion Release Module

UKS: United Kingdom Satellite

---

<sup>0a</sup> Physics department, University of California, Los Angeles, USA

<sup>0b</sup> Rutherford Appleton Laboratory, UK



**ABSTRACT**

Injection of neutral gases into space plasmas has emerged as a powerful technique in reproducing many of the naturally occurring processes in planetary physics in a controlled way. In this article, we present thorough simulation results aimed at explaining and interpreting the AMPTE experiments. The results show the formation of a diamagnetic cavity and a shocklike structure, intense wave activity upstream of the shock, the sideways deflection of the bulk of the AMPTE cloud, the Rayleigh Taylor instability, and the ejection of a tenuous cloud of plasma. All these results are in qualitative agreement with AMPTE observations.

## 1 Introduction

The 1984 AMPTE mission provided a wealth of new results in the area of artificial plasma releases into the solar wind as well as acquiring a new data set on naturally occurring plasma processes. Because the data acquired during the release came from both in situ measurements as well as remote observations, both global and local data were obtained.

The AMPTE experimental data was obtained by two spacecrafts (IRM and UKS) as well as ground based observations and can be divided into three categories.

1. Particle trajectories (local effects): charged particle detection by the spacecrafts; i.e., observation of high energy barium or lithium as well as high energy electrons by the spacecrafts.
2. Wave activity (local effects): magnetic field measurements by the spacecraft magnetometers; i.e., observation of a diamagnetic cavity within the AMPTE cloud, and the generation of wave-like magnetic field configurations in the region in front of it.
3. Cloud motion (global effects): ground based optical observations of the cloud; i.e., observation of protrusions at the head of the cloud as well

as a transverse deflection of the cloud itself.

Most of the lithium measurements were detailed in [Lühr et al., 1986a], [Paschmann et al., 1986], [Häusler et al., 1986], [Gurnett et al., 1986], [Coates et al., 1986], [Hall et al., 1986], while most of the barium measurements in [Valenzuela et al., 1986], [Rees et al., 1986], [Lühr et al., 1986b], [Rodgers et al., 1986], [Woolliscroft et al., 1986], [Haerendel et al., 1986], [Gurnett et al., 1985] and [Klöcker et al., 1988].

Since then, various aspects of the AMPTE results have been the subject of extensive computational and theoretical research. Various mechanisms have been proposed as the basis of the observations. They can be categorized as follows:

1. Recoil of the cloud due to the acceleration of the cloud ions as they are picked up by the solar wind (rocket effect); i.e.. the AMPTE cloud recoils to conserve momentum due to the acceleration of cloud particles at its top by the convective electric field associated with the incoming solar wind. This mechanism was proposed to be responsible for the sideways deflection of the cloud by [Haerendel et al., 1986] and [Cheng, 1987]. Random cloud particle trajectories are needed to examine this mechanism and assess its importance.

2. Asymmetric magnetic field compression; i.e., the asymmetric charging of the cloud and the resulting asymmetric magnetic field compressions surrounding the cloud as likely mechanisms responsible for sideways deflection. This mechanism was also suggested by [Cheng, 1987] and [Brecht and Thomas, 1987]. Magnetic field and density contours should examine this assumption. Kinetic versus MHD simulations would further enrich the analysis and help determine the dominant underlying physics of the complicated interaction.
  
3. The snowplough model; Using a one dimensional hybrid model of kinetic ions and massless fluid electrons developed by [Winske and Leroy, 1984], [Chapman and Schwartz, 1987] obtained magnetic field saturation at the solar wind cloud boundary and showed local momentum coupling between the solar wind and the cloud ions at that boundary, with the momentum gained by the upward moving released (cloud) ions balancing the downward deflected solar wind ions. Thus, [Chapman, 1989] suggested a snowplough mechanism. The model assumes existence of a diamagnetic cavity as an initial condition, and attributes the cloud's motion to the deflected solar wind ions. It does not allow extraction of the cloud ions across the saturated field (snowplough boundary),

presumably due to the one dimensional nature of the model. Random solar wind particle trajectories are needed to examine this mechanism.

4. Electric field in the rest frame of the cloud; this model attributes the sideways deflection of the cloud to an  $\underline{E} \times \underline{B}$  drift where  $\underline{E}$  is the field seen in the release rest frame due to the solar wind. This model was suggested by [Papadopoulos and Lui, 1986]. The electric field arrow plots in the cloud rest frame and the magnetic field contours should examine this assumption.

It is, however, desirable to possess a physical model which can address all the above mentioned effects (particle trajectories, wave activity, cloud motion) and determine which (if any) are important.

Using a hybrid model with kinetic ions and fluid electrons which we believe contains the essential physics, we have been able to reproduce qualitatively the observations. The model also reproduces all the suggested effects (1-4) given above and indicates that all the above mentioned mechanisms are intimately related through the more fundamental physics embodied in the hybrid model.

The initial conditions used in the model most closely resemble the Sept. 20th 1984 lithium releases (the other lithium release was on Sept. 11th 1984).

However, the results obtained are in qualitative agreement in categories 1 and 2 above with both the lithium measurements of the Sept. 1984, and produce the sideways deflection in category 3 that was only observed in the Sunward barium releases of Dec. 1984. Throughout this paper we shall properly reference the measurements as pertaining to the respective releases as we make comparisons with the model; the cloud species will be denoted by (Li) for lithium and (Ba) for barium following each respective reference.

The organization of the paper is as follows. In section two a general picture of the AMPTE releases is presented based on the in situ observations. In section three, the proper simulation form and procedure are discussed. Finally section four is devoted to the outline of the overall simulation results and comparisons with the measurements. The appendix is supplemented as a brief outline of the simulation model.

## 2 Qualitative Analysis

As the cloud ions expand, because of the very high electrical conductivity of the cloud, a diamagnetic cavity is created; a region of compressed plasma and magnetic field is produced at the cloud solar wind boundary which slows

and deflects the incoming solar wind protons. Please see Figure 1 here and Figure 2 of [Haerendel et al., 1986].

As the solar wind approaches the region of compressed magnetic field, the electrons see a strong magnetic field and owing to their small Larmor radii (less than one kilometer) stop drifting into the cloud and form a heated and dense distribution at the cloud boundary, and generate a diamagnetic current [Paschmann et al. 1986] (Li) and [Lühr et al. 1986a,b] (Ba and Li). The ions on the other hand due to their much larger Larmor radii (50 to 500 kilometers, the cloud has a diameter of about 100 kilometers) overshoot and penetrate the region of compressed magnetic field, thus generating an ambipolar electric field ( $\underline{E}_a$ ) which tends to rapidly slow them down; at the same time they are deflected downward by the compressed magnetic field  $\underline{B}$ . The field,  $\underline{E}_a$ , is depicted in Figure 1; it is oppositely directed to the magnetic field gradient. Within the cloud the  $\underline{E}_a$ , however, has the opposite direction to that in the shock region; here it opposes the expansion of the barium ions, [Haerendel et al., 1986] (Figure 2).

In the cloud frame, an observer will measure a convective electric field  $\underline{E}_c = -\frac{1}{c}\underline{v}_{s.w.} \times \underline{B}_0$  [Coates et al., 1986] (Li), [Rodgers et al. 1986] (Ba). This field accelerates ions in the  $+y$  direction in Figure 1; momentum conservation

means there is a  $-y$  pressure on the cloud responsible for its transverse deflection [Haerendel et al., 1986].

At the solar wind cloud boundary, there is all the signatures of a shocklike formation as reported by [Gurnett et al., 1985] (Ba) and [Gurnett et al., 1986] (Li). The following simple jump condition across the shock boundary can be derived using the two fluid and Maxwell's equations, assuming quasi-neutrality and steady state, considering only variations along the  $x$  axis and neglecting electron inertia; i.e. (s.r.  $\equiv$  Shock region, s.w.  $\equiv$  solar wind),

$$[Mnv_x^2]_{s.r.} = -\frac{1}{8\pi} ([B_z]_{s.r.}^2 - [B_z]_{s.w.}^2) + [Mnv_x^2]_{s.w.} \quad (1)$$

We shall use this equation in section 4.2 to compare with our simulation results and thus test all its underlying assumptions.

### 3 The Simulation Model

#### 3.1 The appropriate model

Electrostatic noise, magnetic wave field as well as general plasma wave measurements have revealed the following characteristics about the Ba as well as the Li releases:

1. The plasma wave phenomenon observed in the AMPTE measurements were most intense between the solar wind ion cyclotron and ion plasma frequencies, and sharply dropped at higher frequencies. Using the background solar wind condition of  $B_0 = 10$  nt,  $n_0 = 5/\text{cm}^3$  for the Ba release, [Valenzuela et al. 1986], and  $B_0 = 4$  nt,  $n_0 = 5/\text{cm}^3$  for the Li release, [Häusler et al. 1986], the following range of values for the the ion and electron plasma frequencies, the lower hybrid frequency, the ion and electron cyclotron frequencies, and the Alfvén speed, are obtained respectively:

$$\omega_{pi} \simeq 3 \text{ KHZ} , \omega_{pe} \simeq 134 \text{ KHZ}$$

$$\omega_{lh} \in (16, 41) \text{ HZ}$$

$$\omega_{ci} \in (.4, 1.) \text{ HZ} , \omega_{ce} \in (.7, 1.7) \text{ KHZ}$$

$$C_A \in (40., 100.) \text{ Km/Sec}$$

In this paragraph we shall survey the findings of many authors who had performed wave analysis of the AMPTE data with the above values in mind. [Gurnett et al., 1986] (2nd Li release, Figures 1 and 4) show intense electrostatic noise peaking at 178 HZ with a sharp drop at higher frequencies. [Gurnett et al., 1985] (Dec. 84 Ba release, Figures 3 and

5) also show an almost identical pattern with the Li release. [Häusler et al., 1986] (2nd Li release, Figure 7) on the other hand obtains detailed power spectra of the plasma wave emissions at the time of the maximum wave emissions, one second before the maximum emission, one second after the maximum emission, as well as the prerelease solar wind spectra with all showing the same pattern as above; it thus reveals the most detailed features of the overall AMPTE-plasma behavior and is thus shown here in Figure 4(a). Finally [Wooliscroft et al., 1986] (Dec. 84 Ba release, Figure 1) shows most intense wave activity to occur below 1 KHZ. It is important to note that the above authors did however detect some wave activity at 100 KHZ and above, but at considerably lower intensities. Furthermore some of those high frequency modes were positively identified to be terrestrial kilometric radiation (TKR) or the galactic radio noise (GRN), [Häusler et al., 1986] (Li) and [Gurnett et al., 1985] (Ba).

In conclusion, regarding the electron plasma frequency ( $\omega_{pe} \simeq 134$  KHZ) as the threshold at which electron oscillations and thus inertial effects become significant, most of the observed AMPTE-plasma wave phenomenon falls below that threshold. So neglecting the electron in-

ertia in our physical model should not seriously hinder our effort to simulate the AMPTE releases. Indeed, the physical model used retains some electron dynamics through their  $c\mathbf{E} \times \mathbf{B}/B^2$  drifts, and allows propagation of the whistlers and ion cyclotron waves; i.e., waves that demand electron dynamics, some of which could propagate at rather high frequencies. Additionally, the model allows propagation of the magnetoacoustic, lower hybrid, as well as ion Bernstein modes [Kazeminezhad 1989, 1992a,b].

2. For the problem in which the magnetic field is at right angles to the solar wind flow (2nd Li release), variations along the field line (field draping) can be neglected if they don't qualitatively alter the cloud dynamics; i.e., if the magnetic tensile forces due to the field draping only act in the solar wind direction.

In the Li releases no significant alteration from the above was observed, presumably due to the cloud's rapid expansion and its large radius. For the Ba release also, [Lühr et al., 1986b] reports the magnetic tensile forces to act along the solar wind flow; i.e., in the same direction as the magnetic pressure forces. So the field draping did not qualitatively alter such fine features as the sideways deflection, and according to [Lühr et

al., 1986b], "... the field stresses are still seen to act on a gross scale in the manner expected for larger objects...". Consequently, neglecting variations along the field (using a two dimensional model) should not qualitatively effect the results.

3. Neglecting the displacement current in Maxwell's equations will cause errors of the  $O(c_A^2/c^2)$  [Kazeminezhad, 1992c]. For a plasma in which  $C_A \in (40., 100.)$  KM/SEC in the background and show only increases of  $\leq 10$  in the compressed region, such errors are thus minor.

To sum up; a two dimensional model of kinetic ions and zero mass fluid electrons, neglecting the displacement current, should be sufficient for a qualitative investigation of the AMPTE observations. Details of the model are outlined in the appendix.

### 3.2 The simulation procedure

To model these observations, the model had to incorporate the following features:

1. include the gradual cloud neutral gas ionization in a realistic way.
2. include multiple ion species.

3. include the streaming of the solar wind through the cloud plasma.
4. include the collective behavior of the plasma particles in their self consistent electromagnetic fields.
5. include kinetic effects of the ions; because of their large Larmor orbit size compared to the cloud they must be treated in a kinetic manner.
6. Finally, the code had to handle a very large system because of the complexity and the scale of the interaction.

In the simulations, initially solar wind particles were positioned on a lattice in a regular array moving to the right of the simulation box. The system size was  $256 \times 256$  grids with each grid corresponding to one proton skin depth. New solar wind particles were continually introduced at the left with drift velocities along positive  $x$ , while solar wind particles leaving the box at the right were removed. The cloud particles (mass 6) on the other hand, occupied a circular area centered at the grid point (70 - 128); they are initially neutral and expanding radially and are gradually ionized over one gyroperiod. More specifically, a neutral particle undergoes free streaming at its initial speed, and upon ionization it begins to feel the electromagnetic forces and its motion is then governed by Eqs. 29 and 30 (appendix). Random samples of the cloud

particles are ionized in this way from the neutral bunch once every 1/40th of a gyroperiod. The solar wind field is  $\underline{B}_0 = B_0 \hat{z}$ . Figure 1 contains much of this information.

In the model  $\underline{B}$  and  $\underline{v}$  are normalized according to ( $c_s$  is the ion acoustic speed):

$$\underline{\hat{B}} = \frac{\underline{B}}{\sqrt{4\pi\rho_0}c_s} \quad \underline{\hat{v}} = \frac{\underline{v}}{c_s} \quad (2)$$

Setting  $T_i = 20$  e.v., [Coates et al., 1986], and  $T_e = 15$  e.v., [Paschmann et al., 1986] and [Hall et al., 1986a,b], as the temperatures of the two species in the solar wind, ( $c_s = \sqrt{\frac{T_i+T_e}{M}}$ ) gives  $c_s = 57.9$  Km/sec. Using this  $c_s$  then we obtain the following correspondence of our simulation values of  $v_{s.w.}$  (solar wind particle speed),  $v_{gas}$  (the cloud particle speed) and  $c_A$  (the Alfvén speed) in the MKS units as follows; i.e.,

$$v_{s.w.} = 1.5c_s \cong 86.85 \text{ Km/sec} \quad (3)$$

$$v_{gas} = 0.3c_s \cong 17.37 \text{ Km/sec} \quad (4)$$

$$c_A = 0.15c_s \cong 8.685 \text{ Km/sec} \quad (5)$$

this last value of  $c_A$  also gives rise to an external magnetic field of 0.889 nano-tesla.

The corresponding experimental values are  $v_{s.w.} = 455$  Km/sec,  $v_{gas} = 3.05$  Km/sec, [Coates et al., 1986], with the background  $B_0$  of 4 nano-tesla and proton density of  $5 \text{ cm}^{-3}$ , [Häusler et al., 1986]. These last two values give rise to the measured Alfven speed of 39.04 Km/sec in contrast to our simulation values of 8.7 Km/sec, and the collisionless skin depth of  $\Delta = \frac{c}{\omega_{pi}} \cong 101$  Km which is the unit grid spacing used in the simulations. As will be shown in what follows, these differences between the experimental and the simulation parameters which were imposed by the computational limitations (Courant Fredricks Lewy condition, [Kazeminezhad et al., 1992b]) will have no qualitative effects on the simulation results as one attempts to make comparisons with the measurements.

## 4 AMPTE SIMULATIONS

### 4.1 PARTICLE TRAJECTORIES

The first most significant result was obtained by real space plots of the trajectories of cloud particles in time using the MHD model with the Hall term and the hybrid model respectively. As Figures 2(a) and 2(b) indicate the former represents an isotropic expansion while the latter shows an anisotropic

expansion with sharp upward acceleration only at the top. The latter is much closer to the observations, [Coates et al., 1986] (Li) , [Coates et al., 1988](Ba) and [Haerendel et al., 1986] (Ba), and rules out the treatment of this problem by an MHD approach, even one with the Hall term. The corresponding density contours (Figure 7(a)) closely resemble the experimental contours (Figure 7(c) here , [Haerendel et al., 1986] (Figure 4)), further emphasize this point.

Computer simulations have also yielded excellent depictions of both species of the ion (solar wind and cloud) trajectories. Figure 3(a), representing a selection of solar wind particles flowing in from the left of the simulation box indicates: a downward deflection of those at the bottom of the box due to the sharp magnetic field gradient in front of the cloud. the reflection of some ions at the center indicating the shocklike structure in agreement with the measurements by [Gurnett et al., 1986] (Li) and [Gurnett et al., 1985] (Ba), and almost unperturbed trajectories at the very top; on the whole though they don't indicate immediate downward deflection. Cloud particles (Figure 3(b)) show cycloid type (partial cycloids) trajectories owing to their pick up by the solar wind's convective electric field and their large Larmor radii in agreement with the trajectory measurements of [Coates et al., 1986](Li) and

similar findings by [Coates et al., 1988](Ba) and [Haerendel et al., 1986](Ba).

The magnetic field contours of Figure 1 indicate little symmetry change within one gyroperiod, and it is not until two gyroperiods that they show any significant symmetry changes (Figures 5(a) and 5(b)); i.e., the magnetic field does not undergo rapid symmetry changes. The electric field in the cloud rest frame of Figure 5(c) on the other hand does not indicate a unidirectional field throughout the cloud location ; i.e., for  $x \in (40, 140)$  and  $y \in (40, 180)$  the  $\underline{E}$  does not point consistently along the positive  $x$  to definitely cause an  $\underline{E} \times \underline{B}$  deflection along the negative  $y$ .

As a result, the cloud particle pick up in the solar wind appear to precede the generation of asymmetry in the magnetic field topology and the overall solar wind deflection behind the shocklike region (snowplough boundary), and therefore appear to be the main cause of the cloud's sideways deflection via momentum conservation (rocket effect) as first proposed by [Haerendel et al., 1986] and [Cheng, 1987]. Microscale investigation of the AMPTE results through the study of ion dynamics (e.g., trajectories) thus proved vital, for any global field changes and cloud motion appear to follow their patterns.

The model however being a hybrid one which treats electrons as a fluid does not give electron trajectories or heating. However, the presence of the

high energy electrons observed by the spacecrafts have been probed by investigating the lower hybrid wave activity (i.e., waves which could render electron heating) at the locations both upstream and downstream of the cloud solar wind boundary. We will elaborate on this issue next.

## 4.2 WAVE ACTIVITY

While the convective electric field of the solar wind in the cloud's rest frame plays a significant role in the momentum coupling to the solar wind at the cloud edge, the intense magnetic wave activity induced by the cloud solar wind interaction, plays an equally important role. Indeed from the UKS electron measurements, [Hall et al., 1986] (Li) and [Rodgers et al., 1986] (Ba) concluded electron wave-heating, and in the former they showed the wave-heating to be dominant to the adiabatic compression and electrostatic shock potential difference. The IRM detectors on the other hand detected wave activity in the range of lower hybrid frequencies in the transition region upstream of the cloud [Häusler et al., 1986] (Li); [Wooliscroft et al., 1986] and [Klöcker et al., 1988] (Ba) report similar findings.

Two mechanisms may be responsible for the lower hybrid activity. First, the measurements indicate the generation of a diamagnetic current which is

set up to exclude the solar wind magnetic field from the highly conducting expanding cloud [Lühr et al., 1986a,b] (Li and Ba). These currents can induce what is called the lower hybrid drift instability [Bingham et al., 1991]. This instability can occupy the whole turbulent region, it exists in the region of high ion density and is not suppressed with increasing density. Its only constraint is a threshold velocity for the current carrying electrons which must exceed the ion thermal speed. These lower hybrid drift waves can in turn be absorbed by electrons resulting from Landau damping providing an anomalous resistance and electron heating, [Bingham et al., 1988]. Second it is believed that an instability arising from a two beam (solar wind-cloud particle) situation plays a role in exciting the lower hybrid modes [Papadopoulos et al., 1987]. Since the cloud is photo-ionized by solar radiation and the unionized neutrals freely penetrate into the solar wind, a two stream type situation is produced. We have full dynamic (electron and ion) simulations that show strong electron heating by this mechanism, [Bingham et al., 1988].

These mechanisms are then the likely mechanisms responsible for energizing the electrons in the whole turbulent region, and can therefore explain the observation of large electron energy gain in the cloud and upstream region as reported by the measurements of [Paschmann et al., 1986] (Li) and [Rodgers

et al., 1986] (Ba).

Our hybrid model is rich in its capability for simulating various waves, both fluid-like as well as kinetic-like (Bernstein) [Kazeminezhad et al., 1992a,b]. Using the model we were able to investigate the generation of lower hybrid waves at arbitrary locations in the simulation box. Figures 4(b) and 4(c) show the simulation power spectrum at one location upstream of the cloud and the model's analytic dispersion relation for the lower hybrid waves respectively ( $\pm\omega$  refer to right and left propagations respectively). The value,  $\omega \simeq 0.8$ , in 4(a) agrees with the frequency  $\omega$  in 4(b) for  $k_{\perp} \geq 1$ ; also note the rapid drop in intensity for  $|\omega| \geq \omega_{lh} \simeq .8$  in 4(b) with qualitative agreement to 4(a). Finally Figures 1, 5(a) and 5(b) depicting the magnetic field contours using the 2-d simulations indicate fine scale field configuration, signifying wave activity.

Since the shock generated at the solar wind cloud interaction region is believed to be responsible for both the above instabilities and the resulting wave activity, the simulation model could well investigate this point. For this we shall use the plots of Figure 6. In these plots, the magnetic field, the density and the velocity values at points with fixed  $y$  ( $y = 128$ ), were plotted as a function of  $x$  starting at the right hand of the simulation box

and progressing to its left hand boundary with their abscissa points of 8 and 172 corresponding respectively to the abscissa grid locations 172 and 8 on Figure 1; i.e., straight cut through the cloud.

The plots of Figures 1 and 6(a) illustrate the generation of the diamagnetic cavity within the cloud location (cloud's left boundary falls at the enhanced  $\underline{B}$  field in Figure 1); i.e., in Figure 6(a) one observes a very weak field between the abscissa points 50 and 90 (grid locations 130 and 90 respectively) which is located within the cloud, and a sudden enhancement afterwards (shock region). To sum up then, these plots reveal that; first, the plasma flow does have a component of flow through the cloud as can be seen from Figure 6(c); second, the solar wind velocity does decrease as it flows past the cloud (Figure 6(c) again); third, the existence of the reflected ions as indicated in Figure 3(a) which could also cause a streaming instability by flowing through the solar wind. These effects are in agreement with the findings by [Gurnett et al., 1986] (Li) and [Gurnett et al., 1985] (Ba), and are signatures of a shocklike activity at the cloud solar wind boundary.

To check Eq. 1 against the simulation results, one needs to use the normalizations employed in the model. Using Eq. 2 in Eq. 1 gives:

$$n_{s.r.} \tilde{v}_{s.r.}^2 = -\frac{1}{2} (n_{0s.r.} \tilde{B}_{s.r.}^2 - n_{0s.w.} \tilde{B}_{s.w.}^2) + n_{s.w.} \tilde{v}_{s.w.}^2 \quad (6)$$

where the  $\tilde{v}$  and  $\tilde{B}$  which appear in this equation correspond to the simulation values. We shall drop the tilde from now on. Also  $n_{0s.r.}$  and  $n_{0s.w.}$  correspond to the initial particle numbers (Recall that  $\rho_0 = n_0 M$ , with  $\rho_0$  the density and  $n_0$  the particle number) in the cloud (shock region) and the solar wind regions respectively, and the  $B$ 's are the  $z$  components of the magnetic field. We note the values for the  $B$ ,  $v$  and  $n$  from Figure 6 at the abscissa points 140 and 170 (grid points 40 and 10) and compute the shock jump relation; i.e. Eq. 6:

$$[nv^2] = -\frac{1}{2} [n_0 B_z^2] \quad (7)$$

where

$$[nv^2] = (nv_x^2)_{140} - (nv_x^2)_{170} = -2.20 \quad (8)$$

and

$$-\frac{1}{2} [n_0 B_z^2] = -\frac{1}{2} [(n_0 B_z^2)_{140} - (n_0 B_z^2)_{170}] = -2.23 \quad (9)$$

Note that the initial particle numbers quoted in Eq. 9 arise from the initial conditions; i.e.,  $n_{0s.w.}$  corresponds to 1 particle per cell for the background solar wind particles, and  $n_{0s.r.}$  to 10000 cloud particles in a circle of radius 8 grid points used in the simulations. The results 8 and 9 differ by 1.5% which is very good agreement indeed and supports the theory that a shocklike structure is formed and is responsible for the observed wave activity.

In conclusion, the wave analysis confirm the generation of the lower hybrid waves in the transition region between the diamagnetic cavity and the upstream solar wind in agreement with the measurements by [Häusler et al., 1986] (Li), [Wooliscroft et al., 1986] and [Klöcker et al., 1988] (Ba). The simulations also indicate a shocklike formation at the cloud boundary, presumably as a source for the waves. These waves thus act as a source of energy for the electrons via Landau damping as first suggested by [Hall et al., 1986] (Li) and [Rodgers et al., 1986] (Ba) and explain the observed electron heating in their measurements.

### 4.3 CLOUD MOTION

Ground based optical observations revealed some astounding features of the AMPTE cloud [Valenzuela et al., 1986]. The most important of which were: the cloud's transverse movement across the solar wind flow, the presence of macroscopic protrusions at the top of the cloud, and a tail along the solar wind flow.

This feature was not observed in the Li releases presumably due to the cloud's rapid expansion. In our simulations however, although the Li cloud was used, we do observe this feature. This suggests the same underlying

mechanism, (rocket effect), to be responsible in both cases. Any reference to the Ba measurements serve as purely qualitative.

[Valenzuela et al., 1986] observed that the cloud head did not move in the direction of the solar wind for the first 4.6 minutes. Instead it made a sideways deflection in the negative  $y$  direction at a much lower speed than the solar wind.

The observations relied on the the light emitted from the cloud for tracing its motion. The barium atoms have an energy level which is excited by solar U.V. radiation and which emits visible light. Since the cloud is optically thin the dense parts of the cloud give off the most radiation and only these are recorded: thin dilute regions of the cloud will not be seen. In particular the thin Ba or Li particles ejected upward at very high velocity by the solar wind  $\underline{E}_c$  field will not be seen; however, they were detected by the UKS satellite.

As a result, to model what was observed (the light emitted from the dense part of the cloud), we used the following scheme; the cloud particles' density was counted if it exceeded a certain density; if the density was below this threshold it was omitted. That threshold density was taken to be the density of a single cloud particle per grid cell of scale length  $\Delta = \frac{c}{\omega_{pi}} \simeq 101 \text{ Km}$ ; i.e., the density attributed to a lithium particle in a volume of  $101^3 \text{ Km}^3$ .

Although this choice is arbitrary, qualitatively it should be similar to what is recorded photographically.

Figure 7(b) shows the time history of the  $y$  component of the center of intensity of the heavy part of the "cloud" using this scheme. The pattern shown is similar to what the experimentalists have observed. The cloud does not move for a while (computer time 60 which is roughly 1.5 gyroperiods in the simulations) presumably because not enough particles have been ejected from the top of it to allow a significant recoil of the remaining heavy material. Then suddenly it starts moving down in a relatively short period. Furthermore the protrusions at the top of the Figure 7(a) resemble those of the observations in Figure 7(c).

It has been suggested that the macroscopic protrusions arise from a Rayleigh Taylor type instability driven by the cloud's transverse acceleration: [Hassam and Huba, 1987], [Huba et al., 1987]. The transverse acceleration (across the solar wind flow) in turn was induced by a rocket effect due to the upward ejection of the cloud particles by the solar wind driven convective electric field. The cloud deflection results from momentum conservation as first suggested by [Haerendel et al., 1986] and [Cheng, 1987]. Figure 7(b)'s parabolic shape indicates an acceleration. This accelerating motion could

thus account for the generation of the instability and the resulting protrusions; i.e., as the low density cloud particles get ejected by  $\underline{E}_c$  the dense part recoils (accelerates) in the opposite direction to conserve momentum.

One can think of the heavy fluid composed of the main cloud particles as being accelerated by a lighter fluid which is composed of the solar wind particles and a few cloud ions; one then has the classic Rayleigh Taylor instability taking place. Since the top region is a relatively sharp boundary of the two fluids one can obtain the growth rate to be approximately:

$$\Gamma = \sqrt{k_x a} \quad (10)$$

Here  $k_x$  is just the wave number along the head boundary; i.e., along the  $x$  axis, while  $a$  is the magnitude of the acceleration which points along the negative  $y$  direction.

We shall next use Figure 7 to check Eq. 10. As we see from Figure 7(a) the major fingers at the top are on the average 15 grid points apart along  $x$ ; i.e., the finger wavelength is roughly  $\lambda = 15\Delta$ . From Figure 7(b) on the other hand one sees that the center of mass begins to accelerate at the time  $t = 45$ , and between  $t = 55$  and  $t = 100$  it travels one grid point in the negative  $y$  direction. Thus upon fitting a parabola to that diagram, for a displacement of one grid point in the time period  $\Delta t = 45$ , one obtains an

acceleration  $a = 1.06 \times 10^{-3}$  in the normalized computer units. Given this  $a$  and  $\lambda = 15$  one obtains the growth rate from Eq. 10 to be:

$$\Gamma_1 = \sqrt{\frac{2\pi}{\lambda}} \times a = 2.10 \times 10^{-2} \quad (11)$$

Also for the period of acceleration  $\Delta t = 45$  of the dense part one obtains the following growth rate:

$$\Gamma_2 = \frac{1}{\Delta t} = \frac{1}{45} = 2.22 \times 10^{-2} \quad (12)$$

The Eqs. 11 and 12 agree to within 5.1% which is as good as we can expect from the accuracy of the calculations and lays support to our physical interpretation.

## CONCLUSION

A 2-D kinetic ion and fluid electron model (including ionization) of the AMPTE release experiments confirms the basic concepts of the previous models given by [Haerendel et al., 1986], [Cheng, 1987], [Chapman, 1989], [Papadopoulos et al., 1986]. It thus links all their proposed models (rocket effect, asymmetric magnetic field compression, snowplough and the electric field in the cloud rest frame) and identifies the microscale ion dynamics (e.g., pick up and FLR effects) as the most fundamental underlying mechanism

responsible for the observations. In addition, the observed electron energizations are plausibly accounted for by the lower hybrid wave activity induced by the shock formation and the protrusions at the cloud head by a Rayleigh-Taylor type instability. With computer and computation improvements it should eventually be possible to extend the qualitatively successful modeling presented here to the domain of the quantitative and carry further research in specific subjects of interest.

## A APPENDIX

### THE MODEL

The relevant equations for our particle model are: ( $i$  is the subscript specifying each and every ion).

$$\frac{dr_i}{dt} = v_i \quad (13)$$

$$\frac{dv_i}{dt} = \frac{e}{M_i} \left( \underline{E} + \frac{v_i \times \underline{B}}{c} \right) \quad (14)$$

The massless electrons however satisfy the following equation:

$$\underline{E} + \frac{v_e \times \underline{B}}{c} = 0 \quad (15)$$

where  $v_e$  is the electron fluid velocity. In writing Eq. 15 we assume perfect

conductivity along  $\underline{B}$  e.g.,

$$\underline{E} \cdot \underline{B} = 0 \quad (16)$$

We assume quasi-neutrality to hold; i.e.,

$$n_e = n_i = \int f_i d\underline{v} = n \quad (17)$$

( $n_e, n_i$  are electron and ion densities respectively) where  $f_i$  is the ion distribution function. The current  $\underline{j}$  is therefore :

$$\underline{j} = -en\underline{v}_e + e \int \underline{v} f_i d\underline{v} \quad (18)$$

This current  $\underline{j}$ , according to Eq. 17 (quasi-neutrality assumption) must be divergence free. Thus:

$$\underline{\nabla} \cdot \underline{j} = 0 \quad (19)$$

This also implies that

$$\underline{j}_L = 0 \quad (20)$$

The relevant Maxwell equations are the Faraday's law and the Ampere's law (neglecting the displacement current); i.e.:

$$\underline{\nabla} \times \underline{E} = -\frac{1}{c} \frac{\partial \underline{B}}{\partial t} \quad (21)$$

$$\underline{\nabla} \times \underline{B} = \frac{4\pi}{c} \underline{j} \quad (22)$$

Substituting Eq. 18 into Eq. 22 gives:

$$\underline{j} = \frac{c}{4\pi} \nabla \times \underline{B} = -en\underline{v}_e + e \int f_i \underline{v} d\underline{v} \quad (23)$$

Which then implies:

$$\underline{v}_e = \frac{e \int \underline{v} f_i d\underline{v} - \frac{c}{4\pi} \nabla \times \underline{B}}{ne} \quad (24)$$

As a result using Eq. 15 and Eq. 24 we have:

$$\underline{E} = -\frac{\underline{v}_e \times \underline{B}}{c} \quad (25)$$

$$= -\frac{\underline{B} \times (\nabla \times \underline{B})}{4\pi ne} + \frac{\underline{B} \times \int \underline{v} f_i d\underline{v}}{nc} \quad (26)$$

Finally using Eqs. 21 and 26 we get:

$$\frac{\partial \underline{B}}{\partial t} = c \nabla \times \left\{ \frac{\underline{B} \times (\nabla \times \underline{B})}{4\pi ne} - \frac{\underline{B} \times \int \underline{v} f_i d\underline{v}}{nc} \right\} \quad (27)$$

Using  $\underline{v}'$  as the average ion velocities in a given cell in Eq. 26 gives: (i.e.  $\underline{v}' = \frac{\int \underline{v} f_i d\underline{v}}{n}$ )

$$\underline{E} = -\frac{\underline{B} \times (\nabla \times \underline{B})}{4\pi ne} + \frac{\underline{B} \times \underline{v}'}{c} \quad (28)$$

using Eqs. 14 and 28 gives:

$$\frac{d\underline{v}_i}{dt} - \frac{e}{M_i} \frac{(\underline{v}_i - \underline{v}') \times \underline{B}}{c} = -\frac{e}{M_i} \frac{\underline{B} \times (\nabla \times \underline{B})}{4\pi ne} \quad (29)$$

and upon using Eq. 28 in Eq. 21 we get:

$$\frac{\partial \underline{B}}{\partial t} = c \nabla \times \left\{ \frac{\underline{B} \times (\nabla \times \underline{B})}{4\pi ne} - \frac{\underline{B} \times \underline{v}'}{c} \right\} \quad (30)$$

Eqs. 29 and 30 constitute the basis of our hybrid model. They can be used to derive an analytic dispersion relation, [Kazeminezhad et al., 1992b], the result of which has been used for the Figure 4(c).

A combination of numerical techniques (Lax Wendroff for Eq. 30 and a Leap frog for Eq. 29) coupled with the Richardson extrapolation technique in improving numerical stability have been used in pushing Eqs. 29 and 30. A typical system size was  $256 \times 256$  in the 2-d simulations where each grid point corresponds to one proton collisionless skin depth.

In the MHD Hall term version the second term in Eq. 29 is zero and the pressure term is added instead.

Inclusion of the displacement current leads to corrections of  $O(c_A^2/c^2)$ , [Kazeminezhad, 1992c].

#### ACKNOWLEDGEMENTS

The authors wish to express gratitude to the hospitality of the Rutherford Appleton Laboratory AMPTE-UKS group. In particular useful discussions and insights by Doctors David S. Hall and Duncan A. Bryant should be mentioned. This work was supported by the NSF contract NSF ATM 89-22133, the NATO CGR 910316, and the San Diego Supercomputer SDSC account CLA560.

ADDRESS OF THE AUTHORS

A. FARZAD KAZEMINEZHAD and JOHN M. DAWSON

UNIVERSITY OF CALIFORNIA, LOS ANGELES

PHYSICS DEPARTMENT, KNUDSEN HALL, ROOM 1-130

405 HILGARD AVENUE

LOS ANGELES, CALIFORNIA 90024

PHONE NUMBER(213)825-1787

ELECTRONIC-MAIL ADDRESS

KAZEMINEJAD@UCLAPH.PHYSICS.UCLA.EDU

B. ROBERT BINGHAM

RUTHERFORD APPLETON LABORATORY, CHILTON,

DIDCOT, OXFORDSHIRE, OX11. 0QX, UK

## REFERENCES

- Bingham, R., V.D. Shapiro, V.N. Tsytovich, U. de Angelis, M. Gilman and V.I. Shevchenko, Theory of Wave Activity Occurring in the AMPTE Artificial comet, Phys. Fluids, 3, 1728- 1738, 1991.
- Bingham, R., D. A. Bryant, D. S. Hall, J. M. Dawson, F. Kazeminejad, and J. J. Su, AMPTE Observations and Simulation Results, Comp. Phys. Comm., 49, 257-265, 1988.
- Brecht, Stephen H., V.A. Thomas. Three-Dimensional Simulation of an Active Magnetospheric Release, J. Geophys. Res., 92, 2289-2304. 1987.
- Chapman, S.C., On the Bulk Motion of the Ion Clouds Formed by the AMPTE Solar Wind/Magnetosheath Releases. J. Geophys. Res., 227, 227-240, 1989.
- Chapman, S.C., S.J. Schwartz, One-Dimensional Hybrid Simulations of Boundary Layer Processes in the AMPTE Solar Wind Lithium Releases, J. Geophys. Res., 92, 11059-11073, 1987.
- Cheng, Andrew F., Transverse Deflection and Dissipation of Small Plasma Beams and Clouds in Magnetized Media, J. Geophys. Res.,

- 92, 55-63, 1987.
- Coates, A. J., A. D. Johnstone, M. F. Smith, and D. J. Rodgers, AMPTE/UKS Ion Experiment Observations of Lithium in the Solar Wind, J. Geophys. Res., 91, 1311-1319, 1986.
  - Coates, A. J., D. J. Rodgers, A. D. Johnstone, M. F. Smith., and J. W. Heath., Development of the First Artificial Comet: UKS Ion Measurements, Adv. Space Res., 8, 15-20, 1988.
  - Gurnett, D. A., T. Z. Ma, R. R. Anderson, O. H. Bauer, G. Haerendel, B. Häusler, G. Paschmann, R. A. Treumann, H. C. Koons, R. Holzworth, and H. Lühr, Analysis and Interpretation of the Shocklike Electrostatic Noise Observed During the AMPTE Solar Wind Lithium Releases, J. Geophys. Res., 91, 1301-1310, 1986.
  - Gurnett, D. A., R. R. Anderson, B. Häusler, G. Haerendel, O. H. Bauer, R. A. Treumann, H. C. Koons, R. H. Holzworth, and H. Lühr, Plasma Waves Associated With the AMPTE Artificial Comet, Geophys. Res. Lett., 12, 851-854, 1985.
  - Haerendel, G., G. Paschmann, W. Baumjohann and C.W. Carlson,

- Dynamics of the AMPTE artificial comet, Nature, 320, No. 6064, 720-723, 1986.
- Hall, D. S., D. A. Bryant, C. P. Chaloner, R. Bingham, and D. R. Lepine, AMPTE/UKS Electron Measurements During the Lithium Releases of September 11 and 20, 1984, J. Geophys. Res., 91, 1320-1324, 1986.
  - Hall, D. S., AMPTE/UKS Electron Measurements, private communications, 1986.
  - Hassam, A.B., J.D. Huba, Structure of the Magnetotail Barium Releases, Geophys. Res. Lett., 14, 60-63, 1987.
  - Häusler, B., L. J. Wooliscroft, R. R. Anderson, D. A. Gurnett, R. H. Holzworth, H. C. Koons, O. H. Bauer, G. Haerendel, R. A. Treumann, P. J. Christiansen, A. J. Darbyshire, M. P. Gough, S. R. Jones, A. J. Norris, H. Lühr, and Klöcker, Plasma Waves Observed by the IRM and UKS Spacecraft During the AMPTE Solar Wind Lithium Releases: Overview, J. Geophys. Res., 91, 1283-1299, 1986.
  - Huba, J.D., J.G. Lyon and A.B. Hassam, Theory and Simulation of

the Rayleigh Taylor Instability in the Limit of Large Larmor Radius,  
Phys. Rev. Lett., 59, 2971-2974, 1987.

- Kazeminezhad, F., Hybrid Modeling of Plasmas and Applications to Fusion and Space Physics, UCLA PPG-1261, ph.d. thesis, 1989.
- Kazeminezhad, F., J.N. Leboeuf, F. Brunel, J.M. Dawson, A Discrete Model for MHD Incorporating the Hall Term, in press, J. Comput. phys., 1992.
- Kazeminezhad, F., J.M. Dawson, J.N. Leboeuf, R. Sydora, D. Holland, A Vlasov Ion Zero Mass Electron Model for Plasma Simulations, in press, J. comput. phys., 1992.
- Kazeminezhad, F., Effects of the Displacement current in the low and medium frequencies, private communications, 1992.
- Klöcker, N., H. Lühr, D. J. Southwood and M. H. Acuña, Magnetic Ulf Fluctuations in the Compressional Zone of AMPTE's Artificial Comets, Adv. Space Res., 8, 23-26, 1988.
- Lühr, H., D. J. Southwood, N. Klöcker, M. Acuña, B. Häusler, M. W. Dunlop, W. A. C. Mier-Jedrzejowicz, R. P. Rijnbeek, and M. Six, In

- Situ Magnetic Field Measurements During AMPTE Solar Wind Li<sup>+</sup> Release, J. Geophys. Res., 91, 1261-1270, 1986.
- Lühr, H., D. J. Southwood, N. Klöcker, M.W. Dunlop, W.A.C. Mier-Jedrzejowicz, R.P.Rijnbeek, M.Six, B. Häusler & M. Acuña, In situ magnetic field observations of the AMPTE artificial comet, Nature, 320, No. 6064, 708-711, 1986.
  - Papadopoulos, K., J.D. Huba, A.T.Y. Lui, Collisionless Coupling in the AMPTE Artificial Comet, J. Geophys. Res., 92, 47-54, 1987.
  - Papadopoulos, K., A.T.Y. Lui. On the Initial Motion of Artificial Comets in the AMPTE Releases. Geophys. Res. Lett., 13, 925-927, 1986.
  - Paschmann, G., C. W. Carlson, W. Baumjohann, H. Loidl, D. W. Curtis, N. Sckopke, and G. Haerendel, Plasma Observations on AMPTE/IRM During the Lithium Releases In the Solar Wind, J. Geophys. Res., 91, 1271-1281.
  - Rees, David, Thomas J. Hallinan, Hans C. Stenbaeck-Nielsen, Michael Mendillo & Jeffrey Baumgardner, Optical observations of the AMPTE

artificial comet from the Northern Hemisphere, Nature, 320, No. 6064, 704-708, 1986.

- Rodgers, D.J., A.J. Coates, A.D. Johnstone, M.F. Smith, D.A. Bryant, D.S. Hall & C.P. Chaloner, UKS plasma measurements near the AMPTE artificial comet, Nature, 320, No. 6064, 712-716, 1986.
- Valenzuela, A., G. Haerendel, H. Föppl, F. Melzner, H. Neuss, E. Rieger, J. Stöcker, O. Bauer, H. Höfner & J. Loidl, The AMPTE artificial comet experiments, Nature, 320, No 6064, 700-703, 1986.
- Winske, D., and M.M. Leroy. Hybrid simulation techniques applied to the earth's bow shock. in Computer Simulations of Space Plasmas-Selected Lectures at First ISSS, edited by H. Matsumoto and T. Sato. p. 568, D. Reidel, Hingham, Mass., 1985.
- Woolliscroft, L.J.C., M.P. Gough, P.J. Christiansen, A.G. Darbyshire, H.G.F. Gough, D.S. Hall, D. Jones, S.R. Jones & A.J. Norris, plasma waves and wave-particle interactions seen at the UKS spacecraft during the AMPTE artificial comet experiment, Nature, 320, No. 6064, 716-720, 1986.

- Fig. 1. Magnetic field structure from the simulations after 1 gyroperiod; solid and dotted contours signify fields above and below the solar wind level  $B_0$ . Dotted and dashed paths are a solar wind and a cloud particle trajectory after 2.5 gyroperiods starting at \*'s. The arrows indicate spacecraft paths and field directions.
- Fig. 2. Initial cometary particles after one gyroperiod using the MHD-HALL term model. (b)The same as (a) using the hybrid model.
- Fig. 3. (a)Trajectory of some solar wind particles after 2.5 gyroperiods starting at \*'s. (b)The same as (a) but for cometary particles.
- Fig. 4. (a) Wave power spectra of the 2nd Li release at maximum emission (3), one second before (2) and one second after (4) the maximum, and prerelease (1) [Häusler et al., 1986] (Figure 7). (b)The simulation power spectra at a location inside the cloud. (c) Analytic dispersion relation of the lower hybrid waves ( $\omega$  versus  $k_{\perp}$ ; normalized units).
- Fig. 5. (a)Magnetic field contours after 2.0 proton gyroperiods. (b) Magnetic vector potential contours after 2.0 proton gyroperiods. (c) The electric field arrow plot in the plasma rest frame. The \* and the dashed lines signify the release center and the shock front in (b) and

(c).

- Fig. 6. (a) The simulation cuts of the  $B_z$  at  $y = 128$ , (b) density at  $y = 128$ , (c)  $v_x$  at  $y = 128$  after one proton gyroperiod. These cuts correspond to the data stored along the IRM path shown on Figure 1. (d) Figure 3 in [Haerendel et al. 1986].
- Fig. 7. (a) Simulation density contour from the 2-d model (b) Time evolution of the  $y$  component of the cloud center of mass in 2-d simulations. (c) The experimental density contour. Figure 4 [Haerendel et al., 1986]; compare the 4th, 1st and 2nd panels with 6abc.

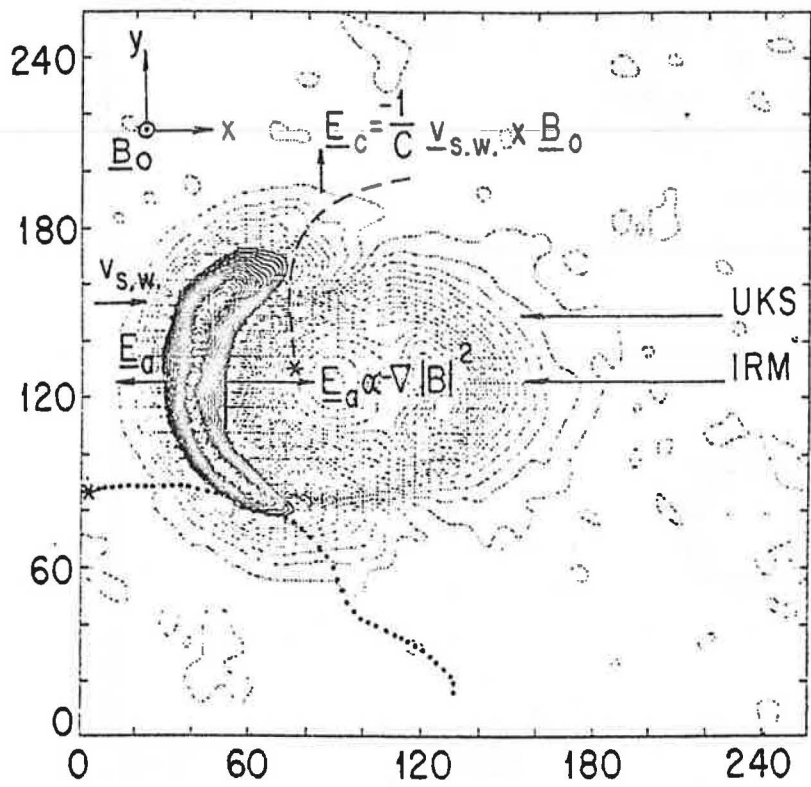


Figure 1

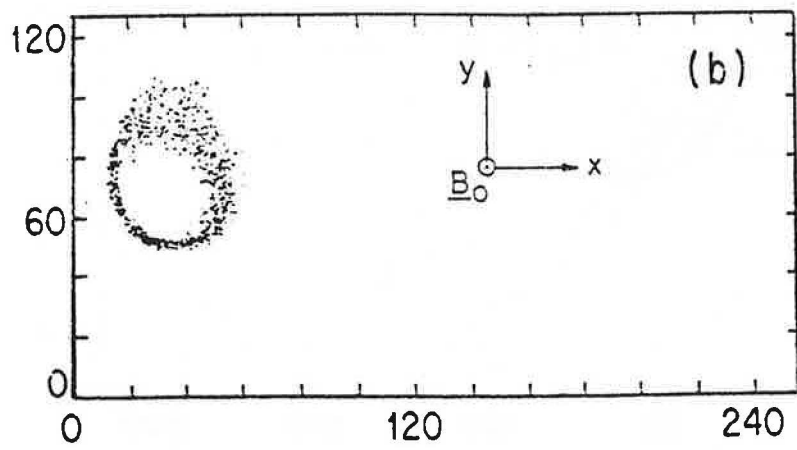
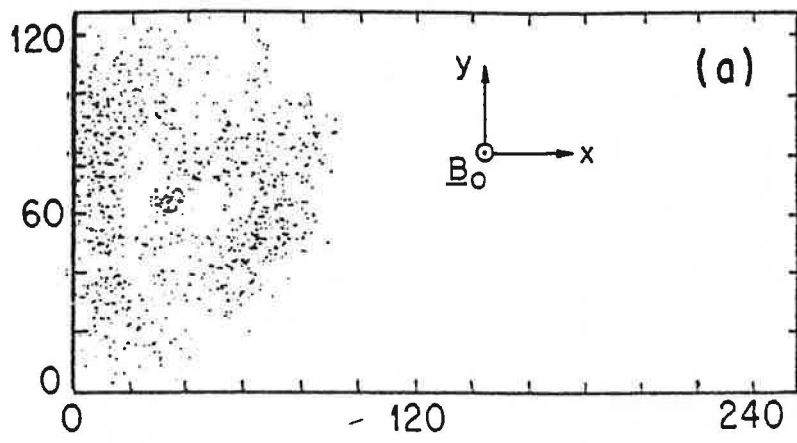


Figure 2

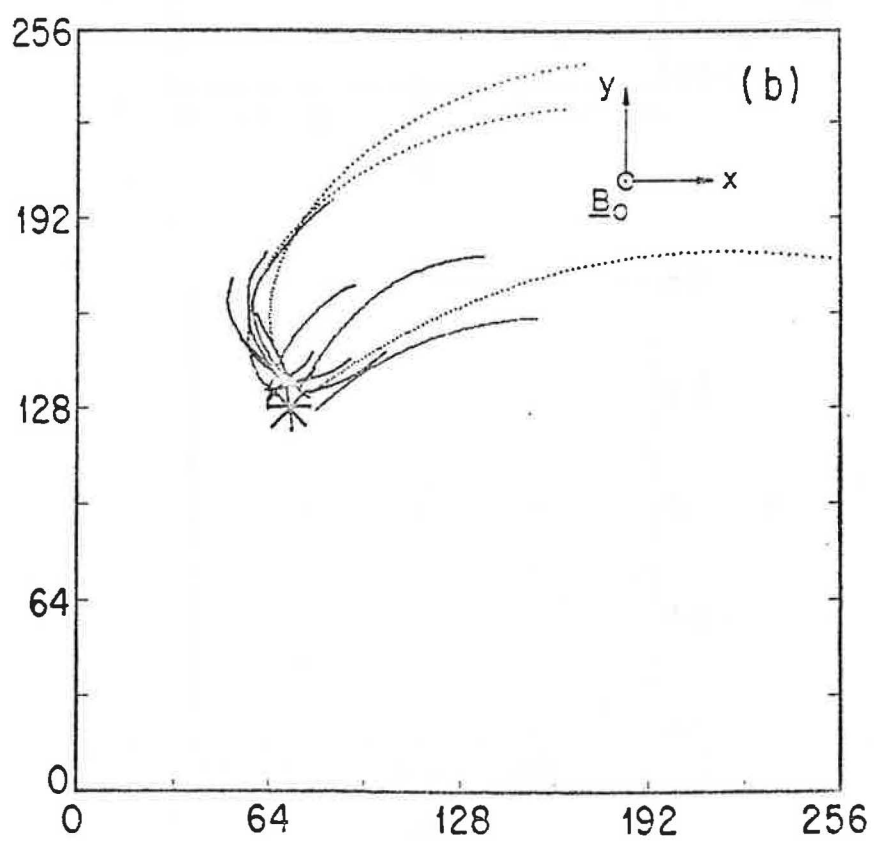
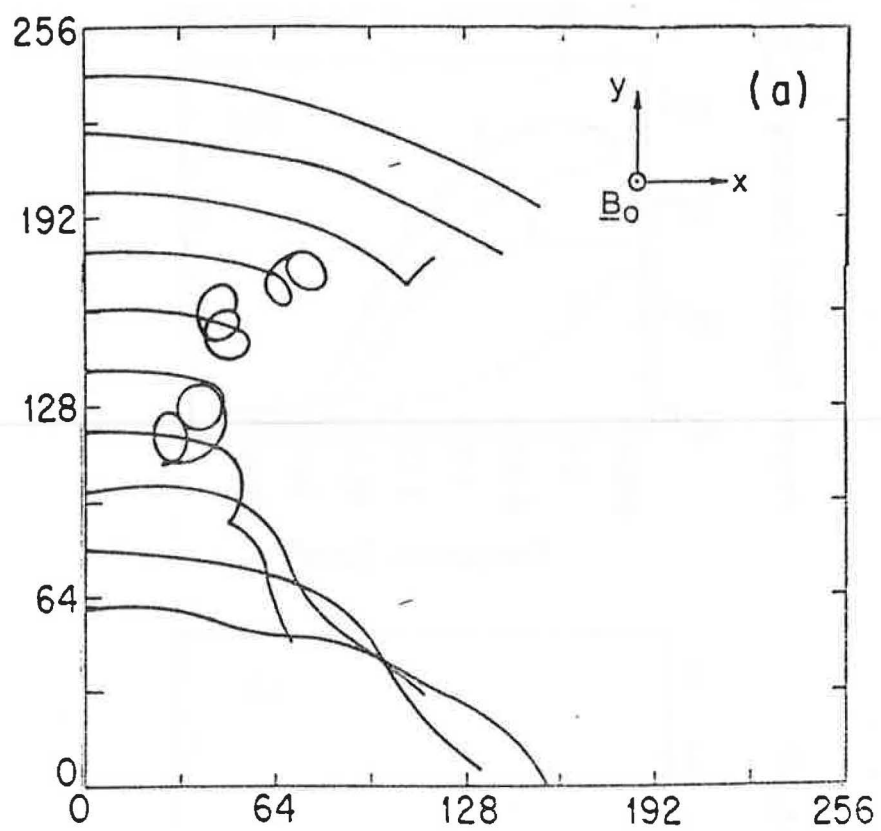


Figure 3

Li - Release #2 Sept. 20. 1984

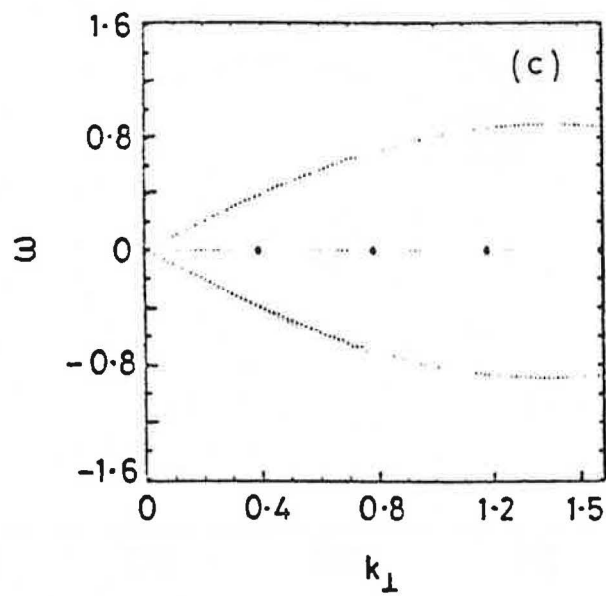
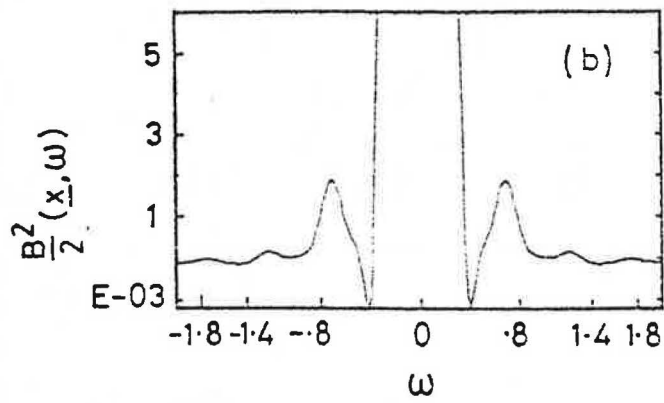
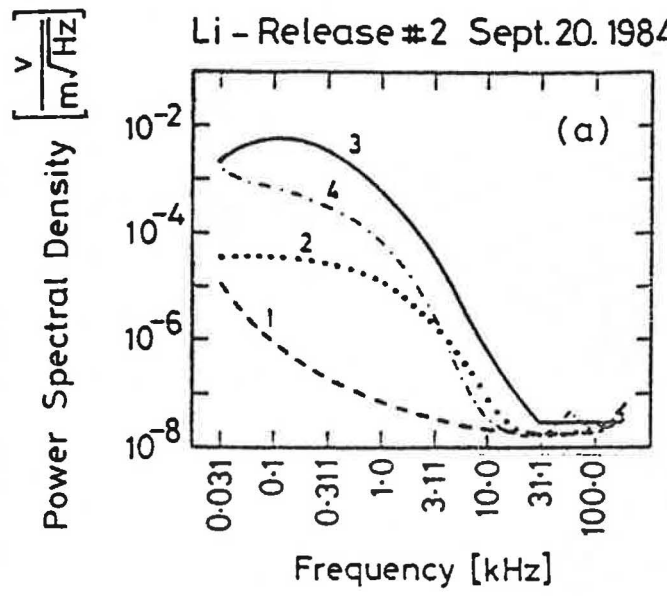


Figure 4

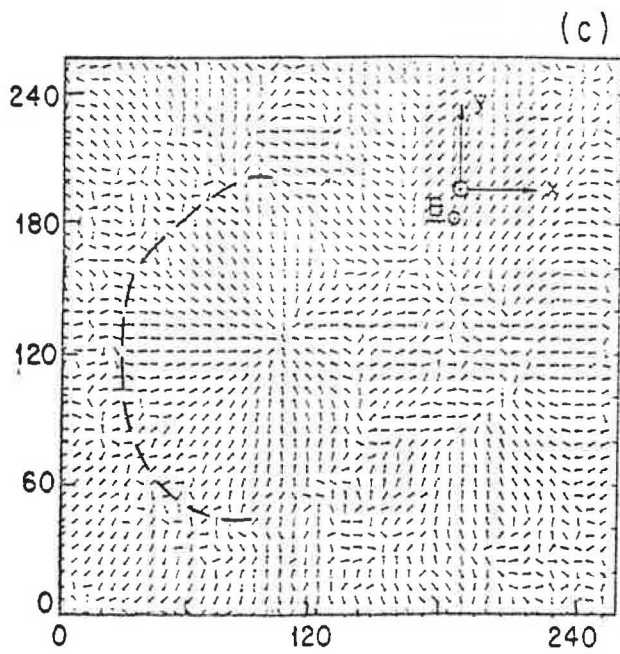
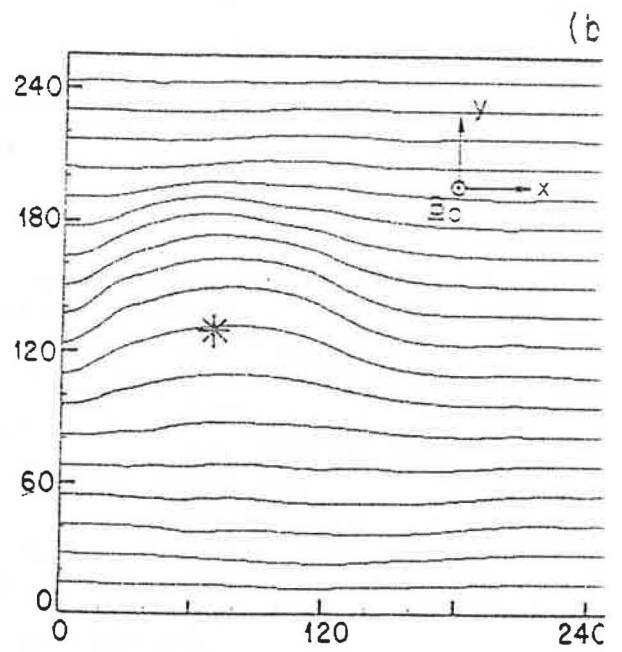
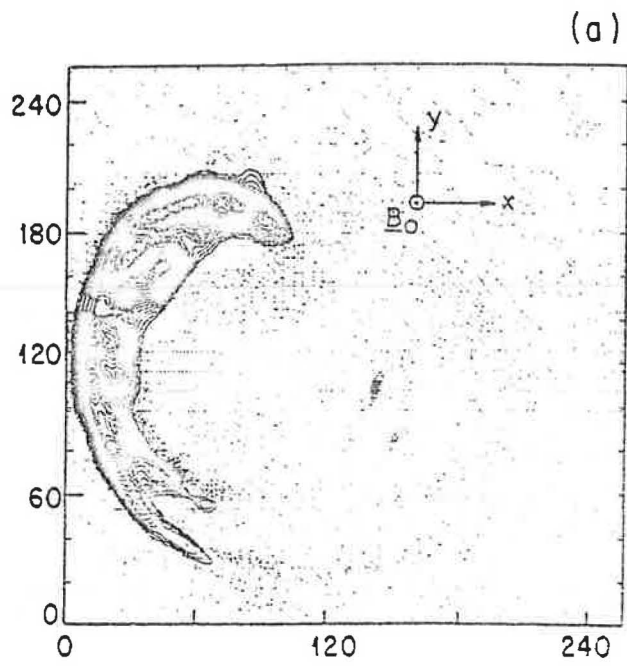


Figure 5

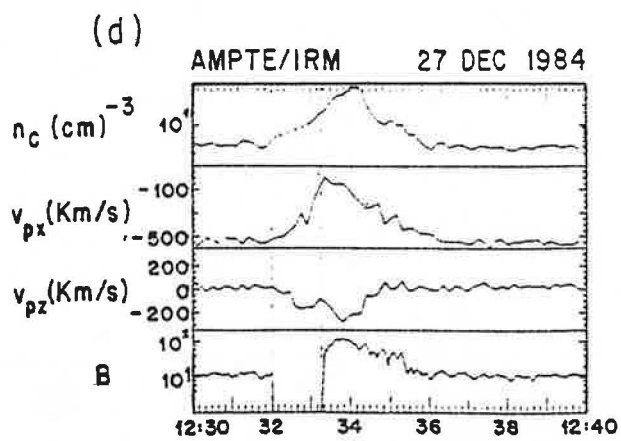
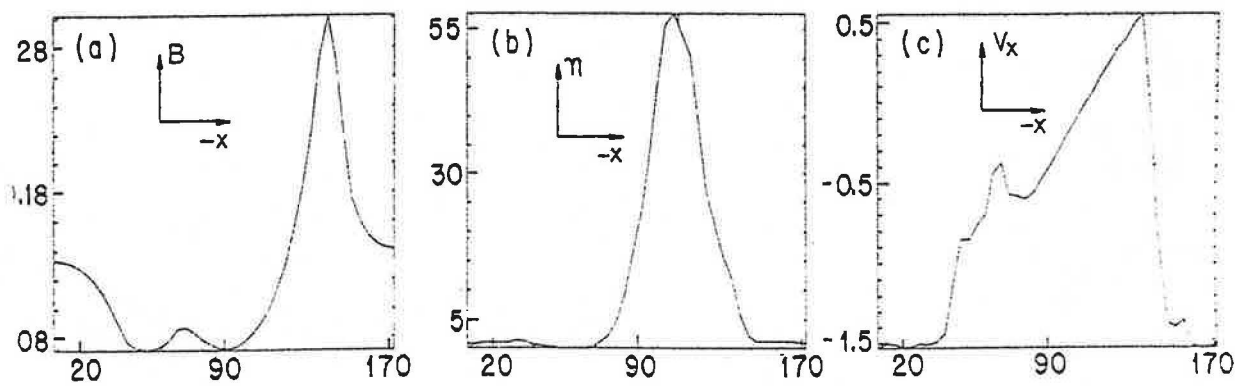


Figure 6

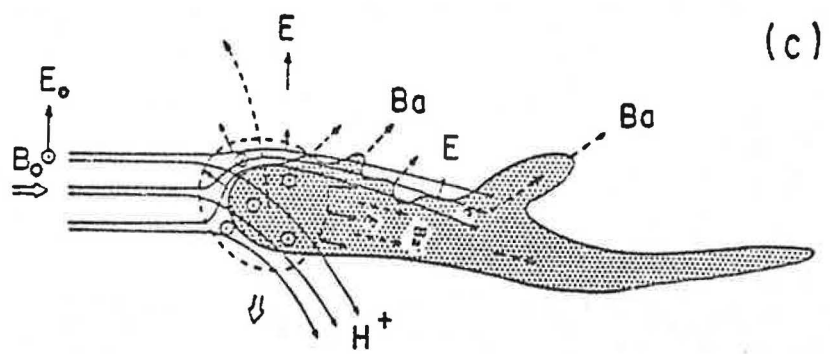
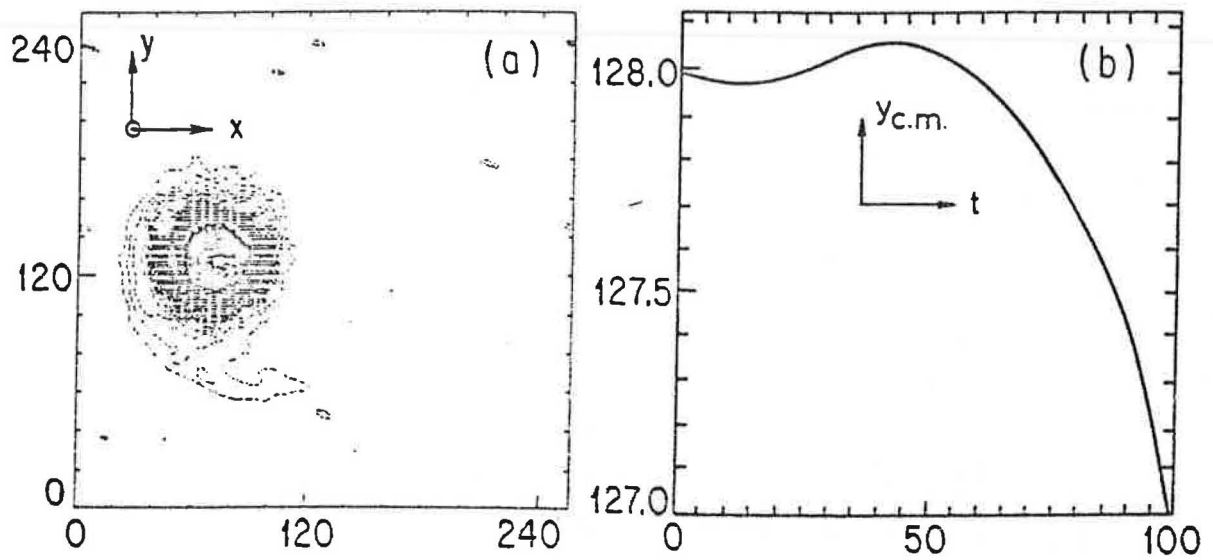
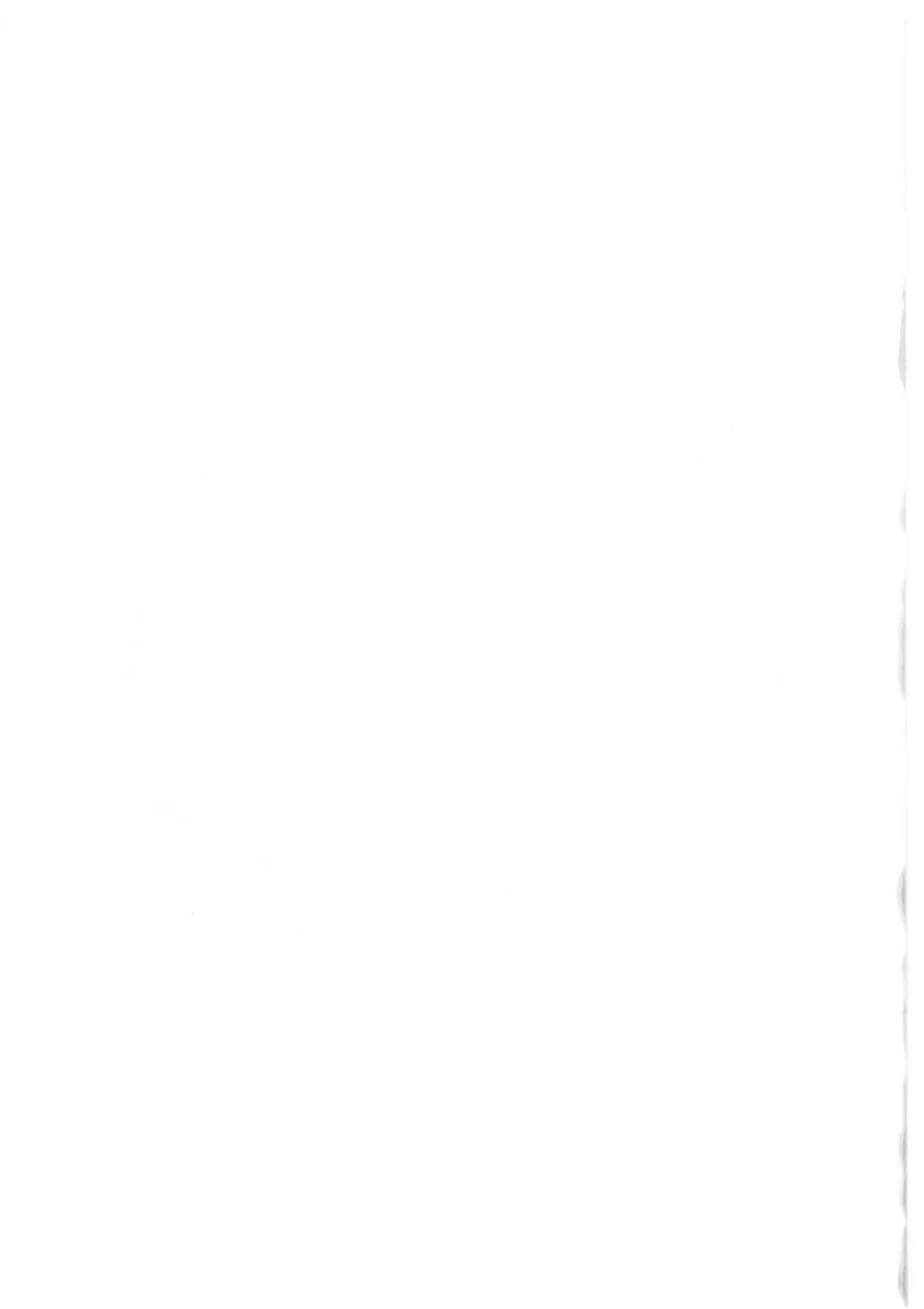


Figure 7



the 1990s, the number of people with a mental health problem has increased in the UK (Mental Health Act 1983).

There is a growing awareness of the need to improve the lives of people with mental health problems. This has led to a number of initiatives, including the development of mental health services, the establishment of mental health charities, and the implementation of mental health legislation.

The aim of this paper is to review the current state of mental health services in the UK, and to discuss the challenges facing mental health services in the future. The paper will first describe the current state of mental health services in the UK, and then discuss the challenges facing mental health services in the future.

The current state of mental health services in the UK is characterized by a number of challenges. These include a shortage of mental health professionals, a lack of resources, and a need for better coordination of services.

The challenges facing mental health services in the future are likely to be even greater. This is due to a number of factors, including an increasing number of people with mental health problems, a growing awareness of the need for mental health services, and a need for better coordination of services.

In order to meet these challenges, mental health services need to be reformed. This will involve a number of changes, including the recruitment of more mental health professionals, the provision of more resources, and the implementation of better coordination of services.

The reform of mental health services is a complex task, and it will require the support of the government, the public, and the mental health profession. However, it is essential that we take action now to improve the lives of people with mental health problems.

The reform of mental health services is a complex task, and it will require the support of the government, the public, and the mental health profession. However, it is essential that we take action now to improve the lives of people with mental health problems.

The reform of mental health services is a complex task, and it will require the support of the government, the public, and the mental health profession. However, it is essential that we take action now to improve the lives of people with mental health problems.

The reform of mental health services is a complex task, and it will require the support of the government, the public, and the mental health profession. However, it is essential that we take action now to improve the lives of people with mental health problems.

The reform of mental health services is a complex task, and it will require the support of the government, the public, and the mental health profession. However, it is essential that we take action now to improve the lives of people with mental health problems.

The reform of mental health services is a complex task, and it will require the support of the government, the public, and the mental health profession. However, it is essential that we take action now to improve the lives of people with mental health problems.

The reform of mental health services is a complex task, and it will require the support of the government, the public, and the mental health profession. However, it is essential that we take action now to improve the lives of people with mental health problems.

the 1990s, the number of people in the UK who are aged 65 and over has increased from 10.5 million to 13.5 million, and the number of people aged 75 and over has increased from 4.5 million to 6.5 million (Office for National Statistics 2000).

There is a growing awareness of the need to address the needs of older people, and the need to ensure that the health care system is able to meet the needs of older people. The Department of Health (2000) has published a strategy for older people, which sets out the government's commitment to older people and the need to ensure that the health care system is able to meet the needs of older people.

The strategy for older people is based on the following principles: (1) to ensure that older people are able to live independently and actively; (2) to ensure that older people are able to access the health care services that they need; (3) to ensure that older people are able to participate in the decisions that affect their lives; and (4) to ensure that older people are able to live in dignity and respect.

The strategy for older people is based on the following principles: (1) to ensure that older people are able to live independently and actively; (2) to ensure that older people are able to access the health care services that they need; (3) to ensure that older people are able to participate in the decisions that affect their lives; and (4) to ensure that older people are able to live in dignity and respect.

The strategy for older people is based on the following principles: (1) to ensure that older people are able to live independently and actively; (2) to ensure that older people are able to access the health care services that they need; (3) to ensure that older people are able to participate in the decisions that affect their lives; and (4) to ensure that older people are able to live in dignity and respect.

The strategy for older people is based on the following principles: (1) to ensure that older people are able to live independently and actively; (2) to ensure that older people are able to access the health care services that they need; (3) to ensure that older people are able to participate in the decisions that affect their lives; and (4) to ensure that older people are able to live in dignity and respect.

The strategy for older people is based on the following principles: (1) to ensure that older people are able to live independently and actively; (2) to ensure that older people are able to access the health care services that they need; (3) to ensure that older people are able to participate in the decisions that affect their lives; and (4) to ensure that older people are able to live in dignity and respect.

The strategy for older people is based on the following principles: (1) to ensure that older people are able to live independently and actively; (2) to ensure that older people are able to access the health care services that they need; (3) to ensure that older people are able to participate in the decisions that affect their lives; and (4) to ensure that older people are able to live in dignity and respect.

The strategy for older people is based on the following principles: (1) to ensure that older people are able to live independently and actively; (2) to ensure that older people are able to access the health care services that they need; (3) to ensure that older people are able to participate in the decisions that affect their lives; and (4) to ensure that older people are able to live in dignity and respect.